Fracture Mechanics of Concrete Structures, de Borst et al (eds) © 2001 Swets & Zeitlinger, Lisse, ISBN 90 2651 825 0

Fracture Modeling with a Microstructural Mechanics Approach

C.S.Chang
Department of Civil Engineering, University of Massachusetts, Amherst, Massachusetts

T.K.Wang
Department of Structural Engineering and Foundation, Polytechnic School of the University of Sao Paulo, SP, Brazil

L.J. Sluys & J.G.M.van Mier
Department of Civil Engineering and Geosciences, Technology University of Delft, the Netherlands

ABSTRACT: Stress-strain relationships have been traditionally derived following a phenomenological approach. Here, we adopt a microstructural mechanics approach to model the development of fracture in concrete. The concrete is assumed to have an underlying microstructure of lattice type. The micro-mechanically based stress-strain relationship is incorporated into a finite element method to evaluate its performance. Uniaxial tensile tests are simulated using different sizes of the finite element mesh. A comparison with experimental results has been studied.

1 INTRODUCTION

Stress-strain relationships used for modeling the mechanical behavior of materials has been traditionally derived following a phenomenological approach, without explicit considerations of the microstructure of the material. Here, we adopt a microstructural mechanics approach to model the development and propagation of fracture in concrete, which is assumed to have an underlying microstructure of lattice type. Although the lattice does not directly reflect the microstructure of concrete, it has been demonstrated as a useful model for the description of concrete fracture (Schlangen & Van Mier 1992, Schlangen 1993, van Mier 1997), in particular when a microstructure is projected on a lattice and corresponding properties are assigned to relevant elements in the lattice. In this microstructural mechanics approach, we aim to derive the stress-strain relationship of the concrete based on the geometrical and material properties of the underlying lattice structure. Since a lattice network of particles can represent a lattice network of beams, we adopt the approach used in granular mechanics (Chang and Liao, 1990, Chang and Ma, 1990, 1991, Chang, 1998, Suiker et. al, 1999, Liao et. al, 2000) to derive the stress-strain relationship for concrete.

In what follows, we first show the relationship between a lattice network of beams and a lattice network of particles. On this basis, the stress-stain relationship is derived for a continuum with underlying lattice structure. Then, the stress-strain relationship is incorporated into a finite element method to simulate specimens under uniaxial tension tests. This is followed by a discussion on the effects of lattice alignment and sizes of the finite element mesh. Predicted results are also compared with experimental results to evaluate the performance and applicability of the model.

2 LATTICE NETWORK

A set of randomly located points can be represented as a lattice network by connecting these points with lines. If the lines are regarded as beams, the lattice network becomes a frame structure, which has been demonstrated as a useful model for the description of concrete fracture (Schlangen 1993, van Mier 1997), in particular when a microstructure is projected on a lattice and corresponding properties are assigned to relevant elements in the lattice.

Alternatively, if the randomly located points are assigned some suitable sizes, they can be considered as a lattice network of particles, which are connected by springs at contact points. The lattice network of particles has been used extensively in granular mechanics to represent a granular medium (Digby 1981, Walton 1987, Cambou et. al. 1995, Chang and Gao 1996). In principle, the representation of a lattice network of beams is equivalent to a lattice network of particles. As schematically shown in figure 1, dashed lines represent the lattice network of beams, which overlay the lattice network of particles. In what follows, we first describe the interaction of two particles in a lattice network. Next we will demonstrate that the behavior of a lattice beam can be represented by the behavior of an equivalent system of two particles connected by springs.

In a lattice network of particles, the movement of a particle can be defined by means of the translation u_i and the rotation ω_i at the particle centroid. The su-

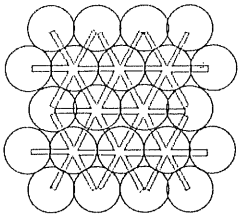

Figure 1. Lattice network of beams and the equivalent lattice network of particles,

per-script 'n' indicates that the movement is refereed to the n-th particle. For two contact particles connected by springs, the relative displacement δ_i^{nm} and the relative rotation θ_i^{nm} between two particles can be obtained from the motion of particles, given as follows:

$$\theta_i^{nm} = \omega_i^m - \omega_i^n \tag{1}$$

$$\delta_i^{nm} = u_i^m - u_i^n + e_{ijk}(r_k^m \omega_j^m - r_k^n \omega_j^n) \tag{2}$$

where the quantity e_{ijk} is the permutation symbol used in tensor representation for the cross product of vectors. The superscript 'n' of the length vector r_i indicates that it is measured from the centroid of particle 'n' to the contact point 'c' of the particles 'n' and 'm'.

The particle interaction can be modeled by two types of spring stiffness: displacement stiffness, and rotational stiffness. The displacement stiffness includes the normal stiffness k_n and the shear stiffness k_s. The rotational stiffness includes the twisting stiffness g_n and the rolling stiffness g_s. The superscript 'nm' shows that the inter-particle properties are referred to the contact of particles 'n' and 'm'.

The relative displacement δ_i and the relative rotation θ_i in Equations (1) and (2) are related to the contact force f_i and the contact moment m_i at the inter-particle contact. A general expression can be given

$$f_i^{nm} = K_{ij}^{nm} \delta_j^{nm} \tag{3}$$

$$m_i^{nm} = G_{ij}^{nm} \theta_j^{nm} \tag{4}$$

in which the contact stiffness tensor K_{ij} and rotation stiffness tensor G_{ij} are the quantities in the global coordinates system. They can be obtained in terms of contact stiffness k_n, k_s, g_n and g_s.

$$K_{ij}^{nm} = k_n^{nm} n_i^{nm} n_j^{nm} + k_s^{nm}(s_i^{nm} s_j^{nm} + t_i^{nm} t_j^{nm}) \tag{5}$$

$$G_{ij}^{nm} = g_n^{nm} n_i^{nm} n_j^{nm} + g_s^{nm}(s_i^{nm} s_j^{nm} + t_i^{nm} t_j^{nm}) \tag{6}$$

where n_i, s_i and t_i are the basic unit vectors of the local coordinate system constructed at each inter-particle contact. The vector n_i is the outward normal to the contact plane. The other two orthogonal vectors s_i and t_i are on the contact plane. In a spherical coordinate system, a vector can be defined by two angles γ and β as in a spherical coordinate system e.g.,

$$\begin{aligned} \vec{n} &= \sin\gamma\cos\beta\,\vec{i} + \sin\gamma\sin\beta\,\vec{j} + \cos\gamma\,\vec{k} \\ \vec{s} &= \cos\gamma\cos\beta\,\vec{i} + \cos\gamma\sin\beta\,\vec{j} - \sin\gamma\,\vec{k} \\ \vec{t} &= -\sin\beta\,\vec{i} + \cos\beta\,\vec{j} \end{aligned} \tag{7}$$

For a two dimensional case ($g_n = 0$) and for two-particles in contact (assuming equal size particles i.e., $r = l/2$), the interaction of two particles can be given as follows in a matrix form

$$\{f\} = [K]\{u\} \tag{8}$$

where the vector $\{f\}$ represents forces f_x, f_y and moment m, and the vector $\{u\}$ represents displacements u_x, u_y and particle rotation ω. The superscripts refer to particle number 1 or 2.

$$\{f\}^T = (f_x^1, f_y^1, m^1, f_x^2, f_y^2, m^2)$$

$$\{u\}^T = (u_x^1, u_y^1, \omega^1, u_x^2, u_y^2, \omega^2)$$

and the matrix $[K]$ is

$$\begin{bmatrix} k_n & 0 & 0 & -k_n & 0 & 0 \\ 0 & k_s & \frac{k_s l}{2} & 0 & -k_s & \frac{k_s l}{2} \\ 0 & \frac{k_s l}{2} & \frac{k_s l^2}{4} + g_s & 0 & -\frac{k_s l}{2} & \frac{k_s l^2}{4} - g_s \\ -k_n & 0 & 0 & k_n & 0 & 0 \\ 0 & -k_s & -\frac{k_s l}{2} & 0 & k_s & -\frac{k_s l}{2} \\ 0 & \frac{k_s l}{2} & \frac{k_s l^2}{4} - g_s & 0 & -\frac{k_s l}{2} & \frac{k_s l^2}{4} + g_s \end{bmatrix} \tag{9}$$

We now compare the stiffness matrix of the two-particle system with that of a beam. For a beam, the stiffness matrix is

$$\{f\} = [M]\{u\} \tag{10}$$

where the vector $\{f\}$ and the vector $\{u\}$ are in the same form as above, except that the forces, moment, displacements and rotation are values at the two ends of the beam.

The stiffness matrix $[M]$ for the beam is given by

$$\frac{E_b I}{l^3}\begin{bmatrix} \frac{A_b l^2}{I} & 0 & 0 & -\frac{A_b l^2}{I} & 0 & 0 \\ 0 & 12 & 6l & 0 & -12 & 6l \\ 0 & 6l & 4l^2 & 0 & -6l & 2l^2 \\ -\frac{A_b l^2}{I} & 0 & 0 & \frac{A_b l^2}{I} & 0 & 0 \\ 0 & -12 & -6l & 0 & 12 & -6l \\ 0 & 6l & 2l^2 & 0 & -6l & 4l^2 \end{bmatrix} \quad (11)$$

where E_b is the Young modulus, I is the moment of inertia, and A_b is the cross section area of the beam.

It is noted that Equations (9) and (10) are identical if the following relationships hold true between the properties of beam and inter-particle springs.

$$k_n = \frac{E_b A_b}{l}; \quad k_s = \frac{12 E_b I}{l^3} \quad (12)$$

$$g_s = \frac{E_b I}{l} \quad (13)$$

Therefore, by selecting appropriate spring constants, the behavior of a two-particle system is identical to that of a beam as schematically shown in figure 2. The cross in the circle between two particles represents the normal, shear and rotational springs.

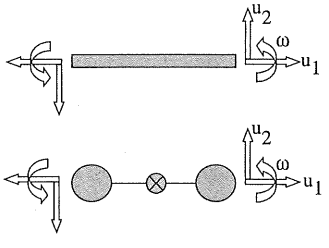

Figure 2. Equivalence of beam and particle systems

3. EQUIVALENT CONTINUUM

A lattice network of beams and a lattice network of particles are discrete systems. We now treat the lattice network of beams as an 'equivalent' continuum and derive the stress-strain relationship of the continuum based on the geometrical and material properties of the lattice structure. Since we have shown that a lattice network of beams can be represented by a lattice network of particles, the approach used in granular mechanics is adopted in the process of homogenization.

We select one regular triangle as a unit cell, which can be conceived as three particles connected by springs. Over the cell, we construct a linear field of displacement and a linear field of rotation.

$$u_i = u_i^o + u_{i,j}^o x_j; \quad \omega_j = \omega_j^o + \omega_{j,p}^o x_p \quad (14)$$

where the superscript 'o' refers to the selected reference point (e.g. the centroid) of the cell (see figure 3). We also define two length measures for the micro-structure of the cell, namely, η_i which represents the length vector from centroid to the i-th side, and l_i which represents the length vector of the i-th side.

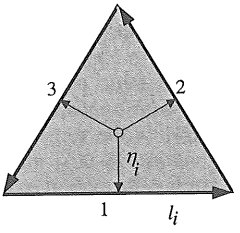

Figure 3. The regular triangle unit cell of a lattice network

Substituting Equation (14) into the kinematic equations of two contact particles (Equations (1) and (2)), it follows

$$\delta_i^c = (u_{i,k}^o - e_{ijk}\omega_j^o) l_k^c - \omega_{j,p}^o e_{ijk} l_k^c \eta_p^c \quad (15)$$

$$\theta_i^c = \omega_{i,j}^o l_j^c \quad (16)$$

Based on Equations (15) and (16), two continuum variables are identified for the cell: the rotation gradient $\omega_{i,j}^{\circ}$ and the 'micro-polar strain' given by

$$\varepsilon_{ki} = u_{i,k}^o - e_{ijk}\omega_j^o \quad (17)$$

which has the same form as those used in the micro-polar model (Eringen 1966) and Cosserat model (Cosserat and Cosserat 1909). Furthermore, using the principle of energy balance

$$\int \left(\sigma_{ij}\varepsilon_{ij} + \mu_{ij}\omega_{j,i}\right) dV = \sum_{c=1}^{3} \left(f_i^c \delta_i^c + m_i^c \theta_i^c\right) \quad (18)$$

the Cauchy stresses and couple stress can be derived as follows:

$$\sigma_{ki} = \frac{1}{V}\sum_c f_i^c l_k^c$$
$$\mu_{pj} = \frac{1}{V}\sum_c \left[-e_{ijk} f_i^c l_k^c \eta_p^c + m_j^c l_p^c\right] \quad (19)$$

and the stress-strain relationship becomes:

$$\sigma_{mq} = C_{mqki}\varepsilon_{ki}^o + D_{mqpj}\omega_{j,p}^o$$
$$\mu_{pj} = D_{pjmq}\varepsilon_{mq}^o + F_{pjri}\omega_{i,r}^o \quad (20)$$

where

$$C_{mqki} = \frac{1}{V}\sum_c K_{qi}^c l_k^c l_m^c$$

$$D_{mqpj} = -\frac{1}{V}\sum_c e_{ijk} K_{qi}^c l_m^c l_k^c \eta_p^c$$

$$D_{pjmq} = -\frac{1}{V}\sum_c e_{ijk} K_{iq}^c l_k^c l_m^c \eta_p^c \qquad (21)$$

$$F_{pjrt} = \frac{1}{V}\sum_c [e_{ijk} e_{qtm} K_{iq}^c l_k^c l_m^c \eta_p^c \eta_r^c + G_{jt}^c l_r^c l_p^c]$$

For a two-dimensional case of a hexagonal lattice network based on regular triangular cells, there are two basic configurations of regular triangles. One is shown in figure 3. The other is in opposite direction of that in figure 3, with the angle pointing downward. For this triangular cell with opposite direction, the stress-strain relationship is the same as Equation (21), except that the values of D_{mqpi} and D_{pimq} have negative signs. If uniform deformation occurs in a region of the hexagonal lattice that covers triangles in opposite directions, the average values of D_{mqpi} and D_{pimq} in Equation (21) are zero.

In order to compare Equation (20) with the conventional form of stress-strain relationship, we define the symmetric and anti-symmetric terms of stress in a two-dimensional case,

$$\tau = \frac{\sigma_{12} + \sigma_{21}}{2};\quad \mathrm{T} = \frac{\sigma_{12} - \sigma_{21}}{2} \qquad (22)$$

We also define the symmetric and anti-symmetric terms of strain

$$\gamma = \varepsilon_{12} + \varepsilon_{21} = u_{2,1} + u_{1,2}\ ;\ \psi = u_{2,1} - u_{1,2}\ ;$$
$$\Gamma = (u_{2,1} - u_{1,2}) - 2\omega = \varepsilon_{12} - \varepsilon_{21} \qquad (23)$$

Note that

$$\varepsilon_{12} = u_{2,1} - \omega\ ;\quad \varepsilon_{21} = u_{1,2} + \omega \qquad (24)$$

The anti-symmetric strain Γ is the relative rotation between rigid body rotation ψ and particle rotation 2ω. The work done by $\tau\,\gamma + \mathrm{T}\,\Gamma$ is the same as that by $\sigma_{12}\,\varepsilon_{12} + \sigma_{21}\,\varepsilon_{21}$. Using the new variables, the stress-strain relationship according to Equation (21) is given in a matrix form by

$$\begin{Bmatrix} \sigma_{11} \\ \sigma_{22} \\ \tau \\ \mathrm{T} \\ \mu_{13} \\ \mu_{23} \end{Bmatrix} = \begin{bmatrix} \frac{2G}{1-\upsilon} & \frac{2G\upsilon}{1-\upsilon} & 0 & 0 & 0 & 0 \\ \frac{2G\upsilon}{1-\upsilon} & \frac{2G}{1-\upsilon} & 0 & 0 & 0 & 0 \\ 0 & 0 & G & 0 & 0 & 0 \\ 0 & 0 & 0 & \Psi & 0 & 0 \\ 0 & 0 & 0 & 0 & \kappa & 0 \\ 0 & 0 & 0 & 0 & 0 & \kappa \end{bmatrix} \begin{Bmatrix} \varepsilon_{11} \\ \varepsilon_{22} \\ \gamma \\ \Gamma \\ \omega_{3,1} \\ \omega_{3,2} \end{Bmatrix} \qquad (25)$$

where G is the shear modulus and υ is the Poisson's ratio. Ψ is the 'spin' modulus, which relates the anti-symmetric part of stress and strain. The value κ is the 'bending' modulus, which relates the rotation gradients and couple stresses. This stress-strain equation is in the same form as the plane stress condition of Cosserat model (see for example, Chang and Ma (1989), Sluys (1992)).

The constants for the equivalent continuum can be related to the spring constants in a lattice spring system or to the beam properties in a lattice beam system.

$$G = \frac{\sqrt{3}}{2}(k_n + k_s) = \frac{\sqrt{3}}{4}\left(\frac{E_b A_b}{l} + \frac{12E_b I_b}{l^3}\right) \qquad (26)$$

$$\upsilon = \frac{k_n - k_s}{3k_n + k_s} = \frac{1 - \left(\frac{h}{l}\right)^2}{3 + \left(\frac{h}{l}\right)^2} \qquad (27)$$

$$\Psi = \sqrt{3}k_s = \frac{12\sqrt{3}E_b I_b}{l^3} \qquad (28)$$

$$\kappa = 2\sqrt{3}g_s + \frac{\sqrt{3}}{6}k_s l^2 = \frac{4\sqrt{3}E_b I_b}{l} \qquad (29)$$

The area A_b is equal to hl. In Equations (26) and (27), the expressions of Poisson's ratio and shear modulus in terms of properties of lattice beams are identical to that given by Schlangen and Garboczi (1997). It is noted that when k_s and g_s are zero, the lattice spring system is reduced to a central force spring network. In that case, the Poisson's ratio is 1/3. When k_s is very large compared to k_n, the Poisson's ratio is close to –1.

For a given element with known modulus and Poisson's ratio, the ratio of h/l can be obtained from Equation (27). Since the size of the underlying lattice structure is known, using Equation (26) the values of all quantities of the underlying lattice structure can be determined: l, h, A_b, I_b and E_b. In the fracture analysis, we also need to know the tensile strength of a lattice beam f_t so that the fracture of a lattice beam can be determined by the axial force of a lattice beam given by

$$F = \left(\frac{E_b A_b}{l}\right)\delta_n \qquad (30)$$

where E_b is the Young's modulus of beams, δ_n is the elongation of the lattice beam. The fracture criterion for a lattice beam is

$$F / A_b \geq f_t \qquad (31)$$

Let ε be the tensile strain of concrete along the direction of a lattice beam such that the elongation

of the lattice beam is εl. Using Equations (30) and (31), the fracture criterion can be rewritten in terms of concrete strain

$$\varepsilon \le \frac{f_t}{E_b} \tag{32}$$

The criterion can also be written in terms of concrete stress $\sigma = E\varepsilon$, which can be deduced as:

$$\sigma \le \frac{E}{E_b} f_t \tag{33}$$

where the limiting value of σ can be considered as the tensile strength of concrete. Note that the criteria in Equations (31-33) depend on the lattice properties.

Since the underlying lattice network has three directions of lattice beams, the fracture criterion has to be checked in all three directions. As soon as the beam reached its allowable tensile strain, it is broken and completely loses its load bearing capacity. No softening law is imposed. The failure criterion is similar to that used by van Mier (1997). It is also noted that the tensile strength of concrete is influenced by the alignment of its underlying lattice structure. Therefore the material is anisotropic.

For example, we assume that the lattice structure is aligned in the same manner as figure 3. After the beam in the second direction has reached its allowable strain, the three load bearing members are now reduced to two. Using Equation (33) and taking the damage of one beam into account, we have the following stress-strain matrix relationship

$$\{\sigma\} = [C]\{\varepsilon\} \tag{34}$$

where

$$\{\sigma\} = (\sigma_{11}, \sigma_{22}, \tau)^T$$

$$\{\varepsilon\} = (\varepsilon_{11}, \varepsilon_{22}, \gamma)^T$$

$$[C] = \frac{\sqrt{3}}{12}\begin{bmatrix} 17K_n + 3K_s & 3(K_n - K_s) & \sqrt{3}(K_n - K_s) \\ & 3(3K_n + K_s) & \sqrt{3}(3K_n + K_s) \\ & & 3K_n + 17K_s \end{bmatrix} \tag{35}$$

It is noted that the stiffness matrix still show a load bearing capacity in the direction in which the beam is broken. The strongest material axis for this damaged material is not perpendicular to the direction of damage. This is a feature that differs from usual damage models.

In the same manner, after the system is stretched more, and assumes additional failure occurs on the second beam in the third direction. The lattice structure now has only one active beam left and the stress-strain matrix is further reduced to

$$[C] = \frac{4\sqrt{3}}{3}\begin{bmatrix} K_n & 0 & 0 \\ & 0 & 0 \\ & & K_s \end{bmatrix} \tag{36}$$

This matrix is singular. The material has now completely lost its load bearing capacity in the direction-2.

4 FINITE ELEMENT ANALYSIS

Based on the model presented above, finite element analyses have been carried out for samples under unaxial tension. Sample of bars (12× 46.765 × 1 mm^3) with three different mesh sizes were considered (l =1mm, l =1.5mm and l =2mm) as shown in figure 4. Each element of the mesh is a regular triangle with an underlying lattice structure aligned in the same way. It is noted that even though the mesh sizes are different, their underlying structure is assumed to have the same size (1 mm in this case). Therefore, we expect the three samples to have the same mechanical response. To start the crack, two weak zones as material imperfections were assigned in the middle of the bar as indicated by the dark areas of Figure 4. For all three samples, the same input material parameters are given as follows: E = 21220 (MPa), ν (Poisson's ratio) = 0.15, f_t = 4.16 (MPa), f_t' =3.16 (MPa) for the weak zones.

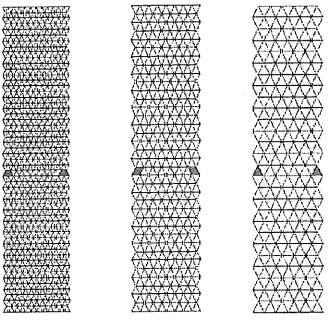

Figure 4. Three different mesh sizes (a) *l=1mm* , (b) *l=1.5mm* and (c) *l=2mm* with horizontal alignment

In a standard continuum damage model, the mesh size has significant effects on the mechanical response, especially after the peak load. Under the uniaxial test conditions, the cracks usually pass through one row of elements, regardless the size of elements used. Therefore, the energy dissipation of the system becomes mesh size dependent, which is the major disadvantage of the usual damage models or smeared crack models (Rots, 1988).

The calculated crack zones from the present finite element analyses are significantly different from the usual damage model. The developed crack bands

are rather wide as compared to the localized cracks in the usual damage model. The presently calculated crack bands cover several rows of elements. The numbers of rows of elements depend on the size of mesh. The patterns and total area of the crack bands are nearly the same for the three meshes.

The width of crack band in the present example is obtained with f_t = 3.16 MPa. for the weak zone. The predicted width of crack band becomes narrower if a smaller value of f_t is used, and vice versa. Therefore the pattern of strain localization is affected by the initial conditions of inhomogeneity. It is noted that even though the crack band is narrower, the bands still cover several rows of elements.

We also observe that for all meshes the mechanical responses are nearly identical. For the three different mesh sizes, the evolution of strain contours during the crack propagation is similar. The strain localization starts to develop from the weak zones, which moves forwards to the middle part of the sample. The small cracks finally coalesce into a major horizontal crack across the mid-section of the bar. The evolution of strain distribution in the longitudinal section is shown in figure 5. From figure 5, it can be observed that the width of the crack band is approximately 14 mm.

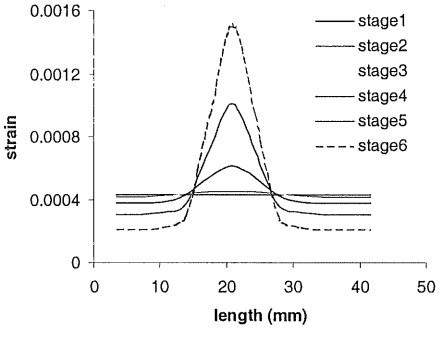

Figure 5. Evolution of strain distribution in longitudinal direction for *l=2mm*

In order to show that the results of the three mesh sizes are nearly identical, we plot the strain variation for the three mesh sizes at a given load level. The strain variations of the three mesh sizes are very close as a typical plot shows in figure 6.

It is commonly known that the stress-strain relationship for the uniaxil test differs depending on the distance of the two points selected for the stress-strain measurement across the crack band. The length between the two selected points is termed as the reference length. For the purpose of proving that the mesh size has no effect on the mechanical response, we have chosen four reference lengths: 7 mm, 14 mm, 21 mm and 46 mm.

We plot the relative displacement of the two points versus the applied load. For a reference length

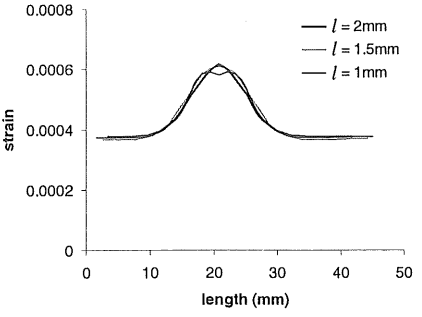

Figure 6. Comparison of strain distribution of the three lattice sizes

equal to 7 mm or 14 mm, the two measuring points are located within the crack band and the strain can be considered as relatively uniform. However, when the reference length is 21 mm or 46 mm, the strain between the two measuring points is not uniform.

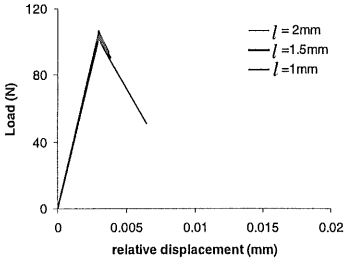

Figure 7. Load-displacement curves for reference length l_{ref} = 7 mm

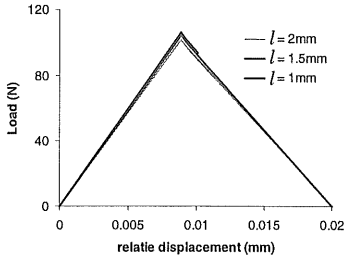

Figure 8. Load-displacement curves for reference length l_{ref} = 21 mm

The load-displacement curves for reference lengths 7 mm and 21 mm are shown in Figures 7 and 8. The results show no sensitivity to the mesh sizes. It is noted that in a conventional damage model, the strain localizes into a single row of elements. The amount of energy release continues to decrease, as the mesh is refined. This type of mesh sensitivity does not reflect the physical reality; it is caused by a loss of ellipticity in governing equation. In the present stress-strain relationship, material instability that occurs after two beams are broken of the triangle

unit in an element (see Equation 34). At the onset of strain localization (i.e, if only the first beam is broken), the system has not yet lost its ellipticity and still has a load bearing capacity. Thus the stress can be redistributed due to the microstructure of lattices, and it avoids the problem of mesh-sensitivity. The present model is found to have a behavior similar to that of a rate-dependent material as observed by Sluys (1992) - the results are mesh-insensitive but sensitive to the initial conditions of inhomogeneity.

It is also noted that the present microstructural approach keeps track of the behavior of the microstructure of the underlying finite elements. There is a conceptual link to an internal length coming from micro-polar properties as the models by Muhlhaus et al. (1987) or from strain gradient models by de Borst et al. (1992, 1995), or non-local models by Bazant et. al (1984) and Pijaudier and Bazant (1987). For these regularized models, the results are not only mesh-insensitive but also insensitive to the initial conditions of inhomogeneity.

In the following case, we simulate the experiments of uniaxial tensile tests on double notched specimens carried out at TUDelft (Shi et. al. 1999). The specimen size is 60×120×10 mm^3 with a notch of 10×2 mm^2. For this analysis, three meshes (872 elements, 1206 elements, and 1664 elements) are used. For the three meshes, the lattice structure alignments are assigned randomly to the finite elements. The results obtained from three meshes are compared to evaluate the effects of the mesh sizes and lattice structure alignment.

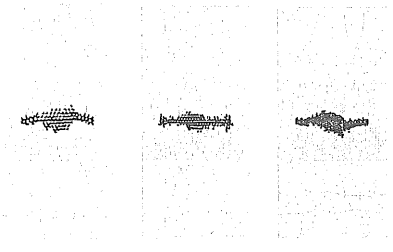

Figure 9. (a) Three mesh discretizations for specimen with double notches

The material parameters used in the analysis are as follows: modulus E = 21220 MPa, Poisson ratio ν = 0.15, tensile strength f_t = 4.16 Mpa. The crack zones of the three specimens obtained from the finite element analyses are shown in figure 9. Due to the effect of random lattice alignments, there are three different crack patterns: the up-curved crack, the straight crack and the s-shape crack. All three patterns resemble the observed crack patterns from different specimens used in the experiments (see Shi et. al. 1999). The randomly aligned lattice structures reflect indirectly the aggregate arrangements in a concrete, thus it is reasonable that different crack paths are produced.

The measured vertical displacement of two points 30 mm across the notches at the left and right edge of the specimen is plotted against load in figure 10. The experimental results are also compared with the computed results from the finite element analysis. According to figure 10, the finite element results show that different mesh discretizations have little influence upon the load-displacement behavior, although the predicted crack patterns are different. The elastic portions of the prediction are nearly identical. The predicted peak loads are very close. The 872-element mesh predicts the smallest peak load, which is approximately 7 % less than the other two meshes.

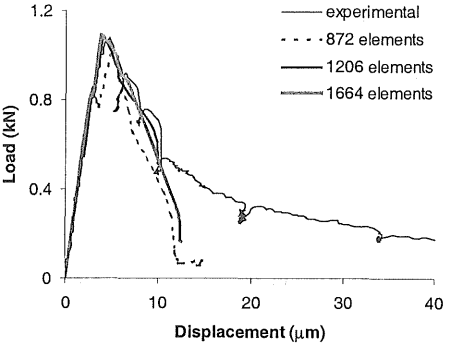

Figure 10. Load-displacement curves of different mesh sizes for specimen with double notch

Near the end of the softening portion of the stress-strain curve, the predicted results show more brittle behavior than the measured results. In the present analysis, the underlying lattice structure within an element is assumed to be uniform and regular, which does not model the detailed heterogeneous microstructures, for example, the formation of crack face bridges. By including the detailed microstructure, it is expected to improve the prediction results of the analysis. Unfortunately, a very fine mesh size is then necessary due to the small scale of the crack face bridges. To avoid the use of a very fine mesh, a more practical solution is to use a phenomenologically based non-linear fracture law for the lattice beam in stead of the purely brittle fracture criterion used in the present analysis

5 SUMMARY AND CONCLUSION

Based on a microstructural mechanics approach, a stress-strain relationship has been derived to model the development and propagation of fracture in concrete, which is assumed to have an underlying microstructure of lattice type. The derived stress-strain relationship is of Cosserat type.

It has been shown in the previous studies that the Cosserat model can achieve the effect of mesh independence in a simple shear test. However, for the uniaxial tensile tests, Cosserate model does not produce the mesh independence effects. In the present study, we show that by considering the underlying microstructure, even in a non-polar model, the finite element results show no sensitivity to the mesh size.

However, the results of the present model are influenced by the alignment of the underlying lattice structure because of the anisotropy in strength. This will lead inevitably that the crack pattern and peak strength are influenced by the microstructure. For simulating a real material, we assume that the lattice alignment in each element is random. For the three specimens in our analyses, we observed that randomly aligned lattice structures in three meshes produce very similar results; the range of peak-load is approximately 7 %, and the computed three types of crack patterns are somewhat different in shape. The three crack patterns however resemble those observed in experimental results. It may be viewed that the alignment of a lattice structure reflects the arrangement of aggregates in concrete; each specimen is indeed somewhat different.

Although this present model belongs to the category of damage models, it has a distinct behavior in that the cracks take place in a wide band as opposed to the narrow crack band typically occurred in a row of elements in the usual damage models. Similar to rate-dependent materials, the present model shows independence on mesh size but a dependency on the initial conditions of heterogeneity of the specimen. The character of the underlying microstructure primarily causes the wider spread of crack band, which is capable of redistributing stress upon strain localization as opposed to usual damage models.

REFERENCES

Bazant, Z.P., Belytschko, T.and Chang, T.P. 1984. Continuum model for strain softening. *Journal of Engineering Mechanics* 110: 1666-1692.

de Borst, R. and Muhlhaus, H.B. 1992. Gradient-dependent plasticity: formulation and algorithmic aspects. *International Journal for Numerical Methods in Engineering* 35: 521-539.

de Borst, R., Pamin, R.H. and Peerlings, R.H.J. and Sluys, L.J. 1995. On gradients-enhanced damage and plasticity models for failure in quasi-brittle and frictional materials. *Computational Mechanics* 17: 130-141.

de Borst, R. and Sluys, L.J. 1991. Localization in a Cosserat continuum under static and loading conditions. *Computer Methods in Applied Mechanics and Engineering* 90: 805-827.

Cambou, B., Dubujet,P., Emeriault, F. and Sidoroff, F. 1995. Homogenization for granular materials. *European Journal of Mechanics A/Solids* 14: 255-276.

Chang, C. S. and Gao, J. 1996. Kinematics and static hypothesis for constitutive modeling of granulates considering particle rotation. *Acta Mechanics* 115: 213-229.

Chang, C. S., and Liao, C. 1990. Constitutive Relations for Particulate Medium with the Effect of Particle Rotation. *International Journal of Solids and Structures* 26(4): 437-453.

Chang, C. S. and Ma Lun. 1990. Modelling of Discrete Granulates as Micropolar Continuum. *Journal of Engineering Mechanics*, ASCE 116(12): 2703-2721.

Chang, C. S., and Ma, L. 1991. A Micromechanical-Base Micro-polar Theory for Deformation of Granular Solids. *International Journal of Solids and Structures* 28(1): pp. 67-86.

Chang, C. S. 1998. Modeling of Granular Materials with Intrinsic Length Scale. *Journal de Physique IV* 8, Pr. 8: 71-78. EDP Sciences, de Courtaboeuf, France.

Cosserat, E., and Cosserat, F. 1909. Theorie des corps Deformables. *Hermann,* Paries.

Digby, P. J. 1981. The effective elastic moduli of porous granular rock. *ASME, Journal of Applied Mechanics* 48: 803-808.

Eringen, A. C. 1966. Linear theory of micropolar elasticity. *J. Math. Mech.* 15: 909-923.

Liao, C.L., Chan, T.C., Suiker, A.S.J., and Chang, C.S. 2000. Pressure-dependent Elastic Moduli of Granular Assemblies. *International Journal for Analytical and Numerical Methods in Geomechanics* 24: 265–279.

van Mier, J.G.M. 1997. *Fracture Processes of Concrete.* CRC Press, Boca Raton (FL).

Muhlhaus, H.B. and Vardolakis, L. 1987. The thickness of shear bands in granular materials. *Geotechnique* 37: 271-283.

Pijaudier-Cabot, G. and Bazant, Z.P. 1987. Nonlocal damage theory. *Journal of Engineering Mechanics* 113: 1512-1533.

Rots,J. G. 1988. *Computational Modeling of Concrete Structure.* Ph.D Dissertation, Delft University of Technology.

Schlangen, E. 1993. *Experimental and Numerical Analysis of Fracture Processes in Concrete.* Ph.D Dissertation, Delft University of Technology.

Schlangen E., and Garboczi, E.J. 1997. Fracture Simulation of concrete using lattice models: computational aspects. *Engineering Fracture Mechanics.* 57(2/3): 319-332.

Schlangen, E. and van Mier, J.G.M. 1992. Experimental and Numerical Analysis of the micromechanisms of fracture of cement-based composites. *Cem.Conc. Comp.* 14(2): 105-118.

Shi, C., van Dam, A.G., van Mier, J.G.M. and Sluys, L.J. 1999. Crack Interaction in concrete. *Conference Proceedings of EUROMAT 99*, Sep. 27-30.

Sluys, L. J. 1992. Wave propagation, localisation and dispersion in softening solids. Ph.D Dissertation, Delft University of Technology.

Suiker, A.S.J., Chang, C.S., deBorst, R, and Esveld, C. 1999. Surface Waves in a Stratified Half Space with Enhanced Continuum Properties, Part-1 - Formulation of the Boundary Value Problem. *European Journal of Mechanics (Solids)* 18: 749-768.

Walton, K. 1987. The effective elastic moduli of a random packing of spheres. *Journal of Mechanics and Physics of Solids* 35: 213-226.